Corrosion Science 78 (2014) 55–62

Contents lists available at ScienceDirect

Corrosion Science

journal homepage: www.elsevier.com/locate/corsci

Duplex stainless steel passive film electrical properties studied by *in situ* current sensing atomic force microscopy

L.Q. Guo [a], M.C. Lin [a], L.J. Qiao [a,*], Alex A. Volinsky [a,b]

[a] Corrosion and Protection Center, Key Laboratory for Environmental Fracture (MOE), University of Science and Technology Beijing, Beijing 100083, People's Republic of China
[b] Department of Mechanical Engineering, University of South Florida, Tampa, FL 33620, USA

ARTICLE INFO

Article history:
Received 29 June 2013
Accepted 30 August 2013
Available online 7 September 2013

Keywords:
A. Stainless steel
B. AFM
B. XPS
C. Passive films

ABSTRACT

The duplex stainless steel passive film electrical properties before and after passivation were investigated by current sensing atomic force microscopy and X-ray photoelectron spectroscopy (XPS). The current maps and band gap energies extracted from I–V curves show that the conductivity of passive film covering austenite and ferrite is different and decreases with increasing film formation potential due to the changes in the passive film thickness and composition, confirmed by XPS analysis. I–V curves reveal that the passive films exhibit *p*-type or *n*-type semiconducting properties depending on the film formation potential, attributed to different film chemical composition, supported by XPS results.

1. Introduction

The corrosion resistance of stainless steel to various corrosive environments is primarily due to the protective passive layers formed on the surface. The changes in passive film and breakdown of passive film directly affect the localized corrosion resistance, leading to pitting, crevice, and intergranular corrosion, along with stress corrosion cracking [1,2]. The passive film properties can vary in terms of the alloy composition, environment, film thickness, structure, stoichiometry, etc. [3,4]. Therefore, investigating passive films local properties is important for understanding the mechanisms of passivity breakdown. Moreover, it is assumed that the breakdown of the passive films on stainless steels is mainly controlled by ionic and electronic transport processes [5–7]. Both of these processes are in part controlled by the electronic properties of the passive film [8–10]. Consequently, the electrical properties are expected to be crucial for understanding the film corrosion resistance characteristics. Recent research of the electronic properties of passive films formed on stainless steels has provided an important contribution for understanding the passive film breakdown mechanisms [11–13]. Several studies at the macroscopic scale indicated that passive oxide films formed on stainless steel are generally composed of two distinct regions of different chemical composition and the semiconductor type [14–16]. However, both chemical and electronic properties of passive films are unlikely to be uniform along the stainless steel surfaces, especially for duplex stainless steels. This is because of a combination of austenite and ferrite phases with a complex microstructure, leading to the differences in corrosion resistance between the two phases [17–19]. Therefore, it is necessary to examine the local characteristics of passive films formed on duplex stainless steel surfaces at the microscopic scale by precise measurements.

Atomic force microscopy (AFM) with a conductive probe can simultaneously characterize both surface topography and the current distribution of passive films with high spatial resolution. By using the current sensing atomic force microscopy (CSAFM), Souier et al. characterized the local electronic properties of the passive film on duplex stainless steel, and demonstrated that the passive film covering austenite and ferrite phases exhibits different properties [20]. They also investigated the effect of surface preparation of 304L stainless steel on electrical conductivity of passive film by CSAFM [21]. However, there is no information available about the semiconducting properties of passive films, including the semiconductor type, which is vital for understanding of mechanisms behind passivity and localized corrosion. Mott–Schottky analysis is widely employed to determine the semiconductor type of the passive film, but it is carried out in the solution at the macroscopic scale, and the results depend on the electrolytic media and the applied potential [22–24]. In order to characterize the semiconductor type and properties of the passive film in air environment at the microscopic scale, a novel measurement approach must be used, which is independent of the measurement conditions, such as the electrolyte and the applied potential.

The present study aims to investigate the semiconducting type and properties of passive films formed in air and at different

* Corresponding author. Address: Key Laboratory for Environmental Fracture, University of Science and Technology Beijing, People's Republic of China. Tel.: +86 10 6233 4499; fax: +86 10 6233 2345.
E-mail address: lqiao@ustb.edu.cn (L.J. Qiao).

0010-938X/$ - see front matter © 2013 Elsevier Ltd. All rights reserved.
http://dx.doi.org/10.1016/j.corsci.2013.08.031

potentials on duplex stainless steel by using CSAFM in air environment. X-ray photoelectron spectroscopy (XPS) was used to characterize the changes in the chemical composition of the passive film.

2. Experimental

2.1. Material and samples preparation

The material used for experiments is conventional 2507 duplex stainless steel, with the chemical composition shown in Table 1, as described in our previous reports [25–27]. The specimens were machined into square sheets with 6 mm × 6 mm × 0.7 mm dimensions. The surface of each specimen was wet ground with SiC paper up to the 2000 grit, and polished using diamond paste to 0.5 μm. Once the mechanical polishing was finished, a final electrochemical etching was performed in a mixed solution of HNO_3:H_2O = 1:1 for 20 s at an applied voltage of 1.2 V, so that the ferrite and austenite phases could be distinguished. Then the specimens were ultrasonically cleaned in ethanol and dried in N_2 gas flow. To identify the scanning region, indentations were made on the surface of each specimen using the digital microhardness tester (HVS-1000) prior to CSAFM measurements.

After surface preparation, specimens were kept for 24 h in air, allowing the formation of a native passive layer. For the formation of passive films, the specimens of 2507 duplex stainless steel were pretreated cathodically at −0.8 V_{SCE} (voltage per saturated calomel electrode), applied for 0.5 h to remove the native oxide film and then polarized in the 0.1 M $Na_2B_4O_7$ solution (pH = 9.2) with a scanning rate of 2 mV/s for 2 h at different film formation potentials. The experiments were carried out at room temperature with the electrochemical cell consisted of specimen as the working electrode, and a saturated calomel and platinum as reference and counter electrodes. Since the passive potential ranges from about −0.2 to 1.1 V_{SCE}, the passive films studied were formed at 0, 0.3 and 0.9 V_{SCE}, representing different potential passive regions.

2.2. Passive film in situ CSAFM measurements

The CSAFM measurements of passive film were performed using Agilent 5500 AFM (Agilent Technologies, USA) operated in the current sensing mode, which measures the surface topography in contact mode along with a voltage applied between the tip and the sample, allowing to obtain topography and current data simultaneously. In addition to topography and current maps, current–voltage (I–V) curves were acquired by setting the probe tip in contact with the passive film at different locations in ferrite and austenite phases of the current maps, which were done at least 10 times at different locations of the specimen, or at different sites of the same locations, to understand the reproducibility. Both current and I–V measurements were carried out in air environment and relative humidity of about 25%. The surface region (80 μm × 80 μm) was scanned at a frequency of 0.1 Hz. The probes used were DPE14/AIBS conductive Pt-coated silicon tips with a force constant of 5.7 N/m and a tip radius of 50 nm.

2.3. Surface analysis

The chemical compositions of the passive films formed in air and at different formation potentials were investigated with XPS using an AXIS ULTRA^{DLD} instrument with a monochromatic Al Ka radiation source with the energy of 1486.6 eV and a pass energy of 40 eV. As for the total energy resolution, the full width half maximum (FWHM) of Ag $3d_{5/2}$ is less than 0.48. The curve fitting was performed using the commercial software XPS Peak, version 4.1, which contains the Shirley background subtraction and Gaussian–Lorentzian tail functions, to achieve better spectra fitting.

3. Results

3.1. CSAFM of the native passive film formed in air

After etching of duplex stainless steel specimen, the ferrite (dark color) and austenite (light color) can be distinguished clearly in optical micrograph, shown in Fig. 1a, which is in good agreement with our previous work [25]. The assignment of phases in the image is further demonstrated by magnetic force microscopy (MFM) image (Fig. 1b) from the area shown in the box in Fig. 1a, where striped magnetic domains can be observed in the region of ferromagnetic ferrite, but not in the paramagnetic austenite. The AFM image (Fig. 1c) on the same area as the MFM image (Fig. 1b), also exhibits the brighter austenite grains and the darker ferrite matrix, and the average height difference between the ferrite and austenite grains is about 50 nm, which is obvious in AFM topography profile, shown in Fig. 1c1.

Fig. 1d shows CSAFM map obtained by applying +0.8 V bias to the probe tip after formation of a native passive layer in air in the same area as MFM and AFM images (Fig. 1b and c). With the aid of AFM and MFM images, the ferrite and austenite phases can be easily distinguished in the current images. Current map indicates that the austenite has a higher current than the ferrite, as shown in Fig. 1d. A line profile in the current map (Fig. 1d1) shows that the current measured on austenite is about 0.23 nA, while on the ferrite it is about 30 pA. The current in austenite obtained at +1.5 V bias has strongly increased compared with the current map obtained at +0.8 V, shown in Fig. 1e and e1. Moreover, the electrical current measured by CSAFM depends on the applied voltage sign, which agrees with the previous reports [28,29]. Compared with the current map obtained with the positive bias (+1.5 V), the current measurements with the negative bias (−1.5 V) display drastic changes of contrast in the current image (Fig. 1f and f1).

3.2. CSAFM of the passive films formed at various potentials

Fig. 2 shows the topography image and the current maps, along with the corresponding current profiles of the passive films formed at 0 V_{SCE} potential in the same scanning region. Compared with the freshly prepared specimen (Fig. 1c), the topography in Fig. 2a remained unchanged, however, the current maps in Fig. 2b–d exhibit significant differences for the same applied tip bias. Although the passive layer on austenite still has higher current than on ferrite, the current drops rapidly on both phases at the same tip bias, i.e.

Table 1
The chemical composition of the 2507 duplex stainless steel.

Phase	Composition in (wt.%)							
	C	Cr	Mn	Fe	Ni	Mo	N	S
α	0.011 ± 0.001	28.59 ± 0.17	0.66 ± 0.09	61.59 ± 0.31	5.06 ± 0.12	5.04 ± 0.07	0.06 ± 0.01	0.002 ± 0.001
γ	0.012 ± 0.001	25.72 ± 0.16	0.81 ± 0.09	62.40 ± 0.31	7.15 ± 0.12	3.75 ± 0.06	0.59 ± 0.01	0.001 ± 0.001

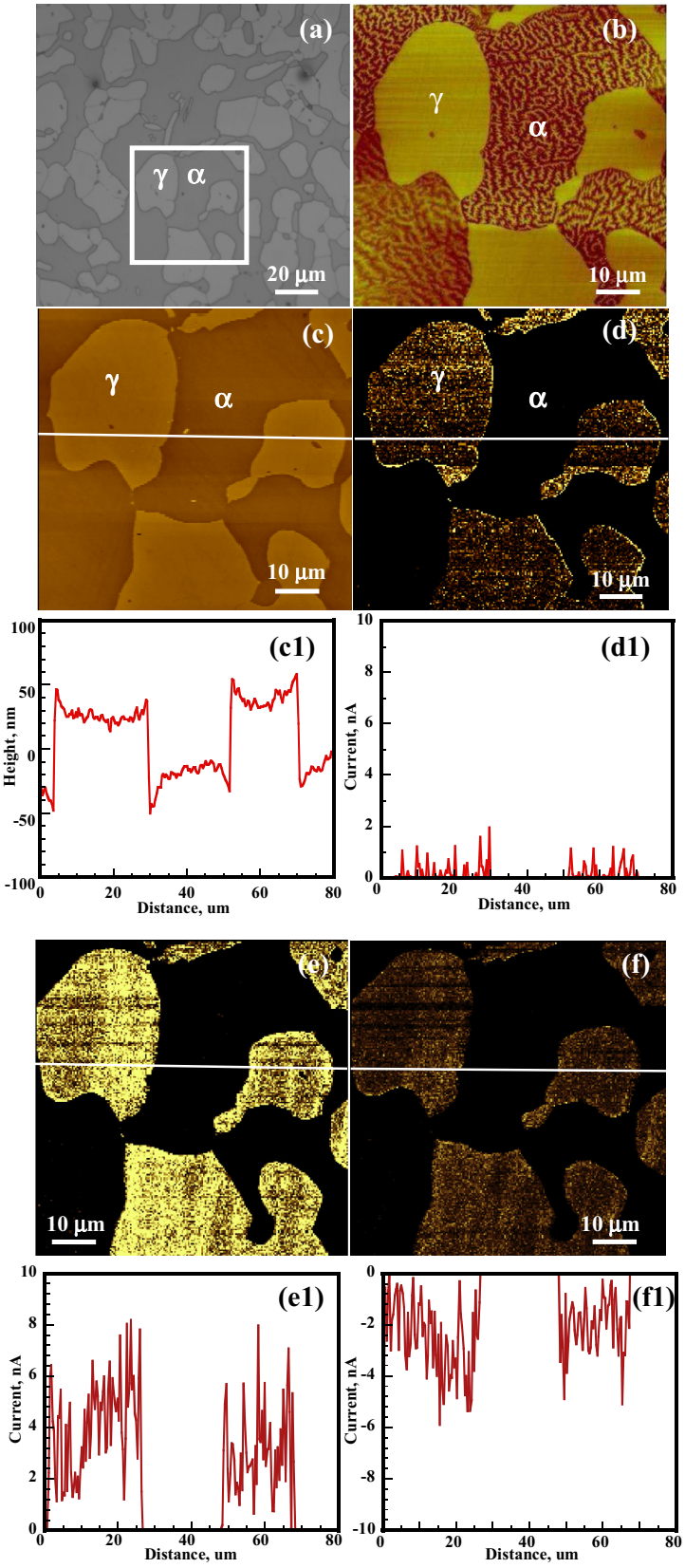

Fig. 1. (a) Optical micrographs of the 2507 duplex stainless steel specimen electrochemically etched with air-formed film on the surface; (b) MFM image of the boxed area in (a); (c) AFM topography on the same region as (b); (c1) AFM topography profile of a line shown in (c), and corresponding conductive maps for: (d) +0.8 V; (e) +1.5 V and (f) −1.5 V applied tip bias. (d1), (e1) and (f1) are line CSAFM current profiles shown in (d), (e) and (f).

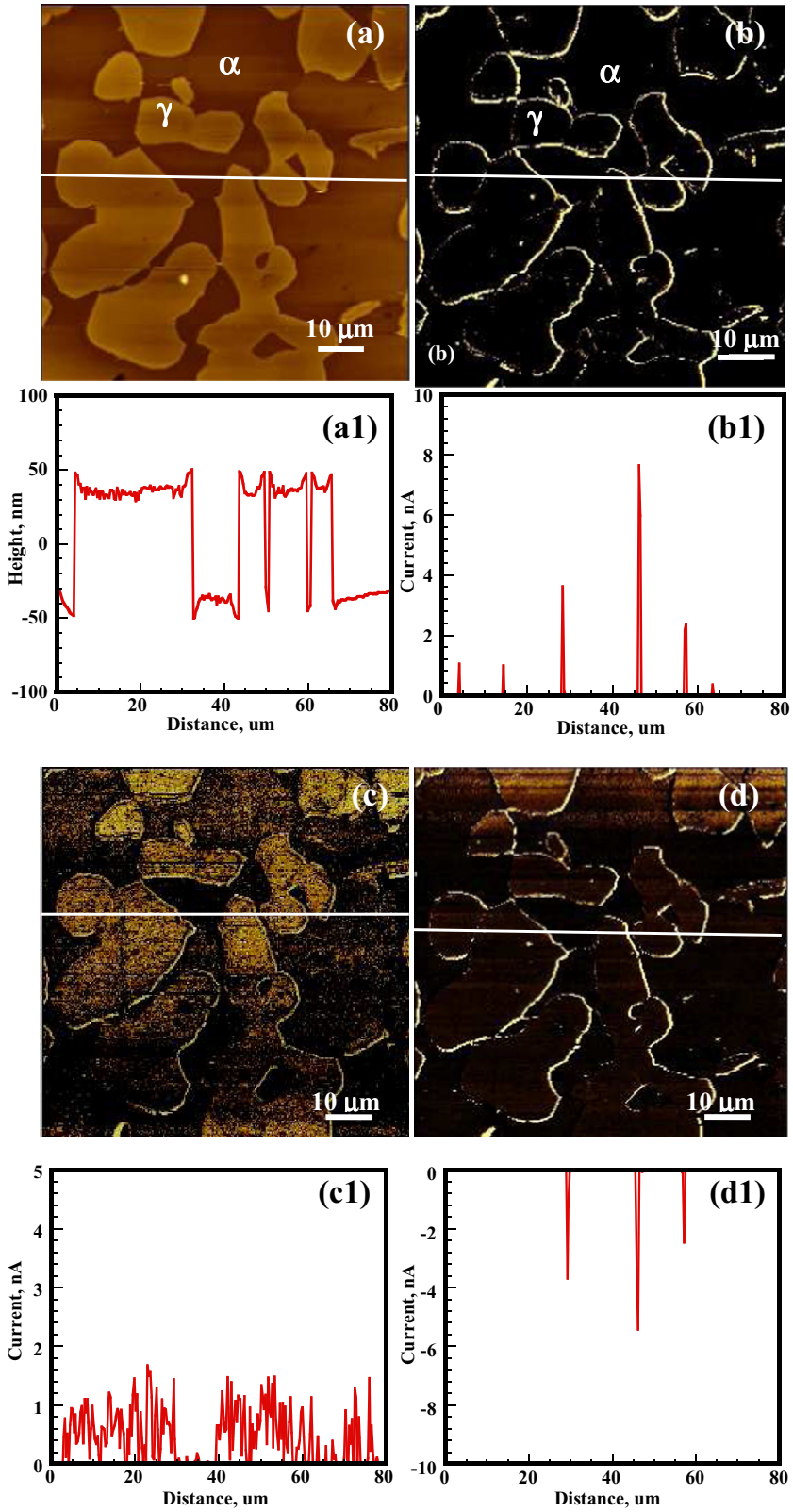

Fig. 2. (a) AFM topography image on the passive film formed at 0 V_{SCE} potential and the corresponding current maps for: (b) +0.8 V; (c) +1.5 V and (d) −1.5 V applied tip bias, (a1) AFM topography line profile, as shown in (a). (b1), (c1) and (d1) are line current profiles shown in (b), (c) and (d).

the passive film formed at 0 V_{SCE} becomes more insulating than the one formed in air, which is obvious from the current line profiles. The current obtained at +0.8 V bias in the austenite is about 40 pA, while in the ferrite is about 20 pA (Fig. 2b and b1). The current in austenite obtained at +1.5 V bias has increased compared with the current map obtained at +0.8 V, shown in Fig. 2c and c1. Similar results are obtained for the passive films formed at 0.3 and 0.9 V_{SCE}. Table 2 lists the average current values in the passive

Table 2
Average current in nA measured by CSAFM of the passive films formed on the ferrite and austenite phases of 2507 duplex stainless steel in air and after passivation at 0 V_{SCE}, 0.3 V_{SCE} and 0.9 V_{SCE}.

Passive film	Phase	Applied tip bias (V)		
		0.8 V	1.5 V	−1.5 V
In air	γ	0.239 nA	3.7 nA	−2.32 nA
	α	0.031 nA	0.063 nA	−0.038 nA
After passivation				
0 V_{SCE}	γ	0.043 nA	0.66 nA	−0.05 nA
	α	0.02 nA	0.126 nA	−0.025 nA
0.3 V_{SCE}	γ	0.022 nA	0.35 nA	−0.031 nA
	α	0.011 nA	0.13 nA	−0.016 nA
0.9 V_{SCE}	γ	0.015 nA	0.17 nA	−0.22 nA
	α	0.006 nA	0.05 nA	−0.09 nA

films over the austenite and ferrite phases formed in air and at various potentials. The current decreases after passivation at various potentials, and drops sharply with the increase of the film formation potential. The highest current is obtained from the passive film formed in air, and the lowest from the passive film formed at 0.9 V_{SCE}. The passive films on duplex stainless steel exhibit semiconducting behavior.

3.3. Passive films I–V characteristics

To further examine electric characteristics, the I–V curves were measured on the passive films at different tip positions in both phases. Fig. 3 shows a series of I–V curves on the passive films covering the austenite and the ferrite phases formed in air and at different potentials. The I–V curves reveal that the austenite grains have higher conductivity than the ferrite, and the passive films formed in air has better conductivity than those formed at various potentials. Also, the conductivity decreases sharply with the film formation potential. This is consistent with the current maps of the passive films shown in Figs. 1 and 2 and in Table 2. Moreover, the zero-current region width on ferrite is much larger than that on austenite, and the zero-current regions on both phases become wider with the film formation potential, indicating that the passive films become more insulating.

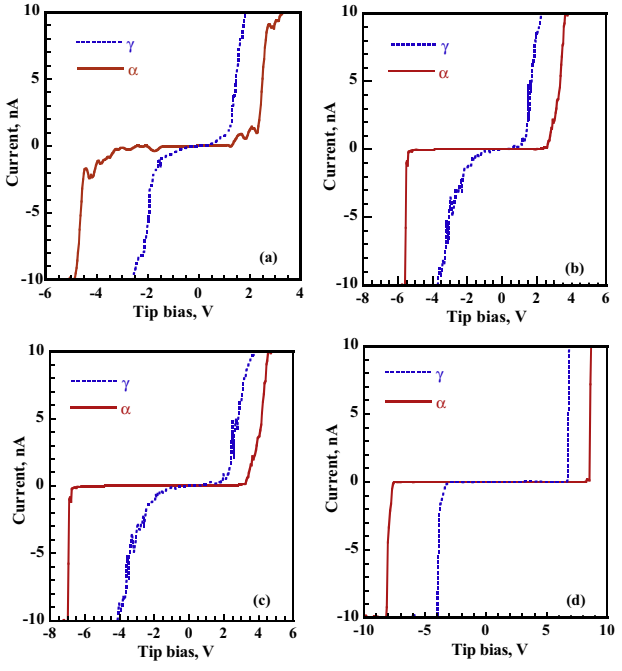

Fig. 3. Typical I–V curves obtained from the passive films on the ferrite and austenite phases formed on 2507 duplex stainless steel in air (a), and after passivation at 0 V_{SCE} (b), 0.3 V_{SCE} (c) and 0.9 V_{SCE} (d).

It is worth noting that the I–V curves either on ferrite or austenite phases are asymmetric. For CSAFM measurements the tip is kept in contact with the semiconducting passive film surface, so metal–semiconductor–metal contacts are present between the Pt-coated tip, the passive film, and the steel substrate. The asymmetric shape of the I–V curves implies that both the tip and the semiconducting passive film and the metal substrate and the semiconducting passive film both form Schottky junctions. It is well known that in case of direct contact between the metal and the semiconductor (both *n*- and *p*-types), the low resistance corresponds to the majority carriers flow from the semiconductor to the metal. If the voltage bias is positive, the holes act as the majority carriers for the *p*-type semiconductor, flowing from the semiconductor to the metal, which is a low resistance path, corresponding to the higher current values. However, if the bias is negative, the holes should flow from the metal to the semiconductor, which is the high resistance path, resulting in smaller current. If the tip bias is negative, electrons act as the majority carriers for the *n*-type semiconductor, moving from the semiconductor to the metal, which is the low resistance path, thus the measured current is higher. On the contrary, when the bias is positive, the measured current is lower. Therefore, the semiconductor type of the passive films is determined according to the I–V curves in Fig. 3. The passive films formed in air, and at 0 or 0.3 V_{SCE} are *p*-type semiconductors, and the film formed at 0.9 V_{SCE} is the *n*-type semiconductor.

3.4. XPS passive film analysis

XPS analysis was carried out to examine the change in the film surface composition caused by passivation, as shown in Figs. 4–7, where both metallic and oxidized states of Fe $2p_{3/2}$, Cr $2p_{3/2}$, Ni $2p_{3/2}$ and Mo 3d are present. The FWHM for the oxide peaks were fixed to be the same and the FWHM applied for the metallic components was taken from the corresponding metal, being measured after the surface oxides were removed. The binding energies used in the spectra from the XPS measurements are used according to the NIST database and previous reports [30–34]. After background subtraction, according to Shirley, the XPS results are separated into contributions of the different oxidation states by a fit procedure described in previous reports [33–35]. Spectra deconvolutions of the passive film primary compounds (iron, chromium, molybdenum and nickel) are performed based on the corresponding binding energies, listed in Table 3. The spectra for the passive films formed in air and at 0 or 0.3 V_{SCE} potentials represent almost the same film composition (see Figs. 4–7). The Fe $2p_{3/2}$ signals in Fig. 4 shows the presence of the three components: metallic state ($Fe_{(met)}$, 706.5 eV), the bivalent (Fe^{2+}) and the trivalent (Fe^{3+}) species. The relative peak heights of Fe_2O_3 (711.5 eV) show that Fe^{3+} is the primary iron oxidized species in the passive film. The concentration of $Fe_{(met)}$ decreases, while Fe_2O_3 contents increase by passivation, and this change happens faster at higher potential. For the Cr $2p_{3/2}$ spectra in Fig. 5 there are three constituent peaks, representing to $Cr_{(met)}$ (573.8 eV), $Cr(OH)_3$ (577.0 eV) and Cr_2O_3 (576.0 eV). The $Cr_{(met)}$ concentration is reduced with the applied potential, while the $Cr(OH)_3$ and Cr_2O_3 contents are increased, especially at 0.3 V_{SCE} potential, there is no Cr peak. The Ni $2p_{3/2}$ spectra in Fig. 6 represent the metallic state ($Ni_{(met)}$, 852.3 eV), along with $Ni(OH)_2$ (855.78 eV) and NiO (854.02 eV). The concentration of $Ni_{(met)}$, $Ni(OH)_2$ and NiO contents are changed with the applied potential. Mo 3d spectra in Fig. 7 indicate the metallic

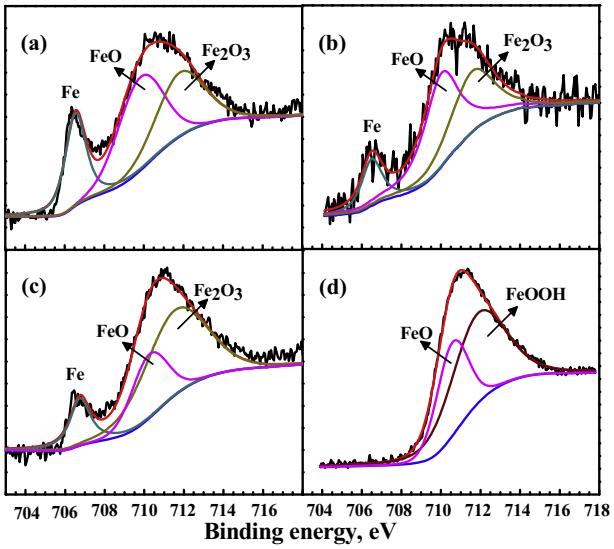

Fig. 4. XPS spectra of Fe $2p_{3/2}$ of the passive film formed on 2507 duplex stainless steel in air (a), and at 0 V_{SCE} (b), 0.3 V_{SCE} (c) and 0.9 V_{SCE} (d) potentials.

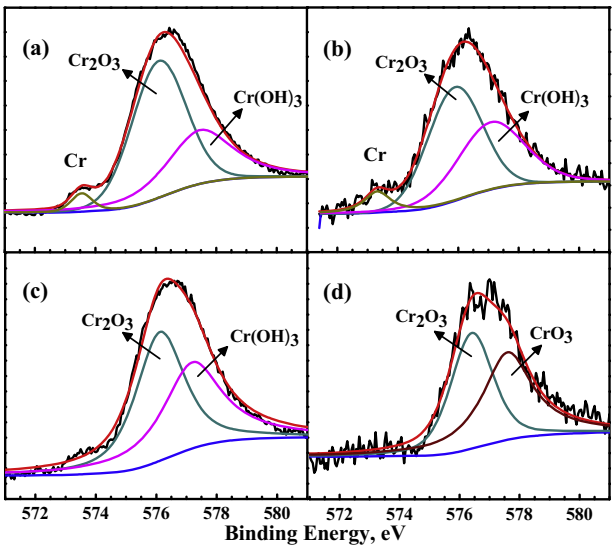

Fig. 5. XPS spectra of Cr $2p_{3/2}$ of the passive film formed on 2507 duplex stainless steel in air (a), and at 0 V_{SCE} (b), 0.3 V_{SCE} (c) and 0.9 V_{SCE} (d) potentials.

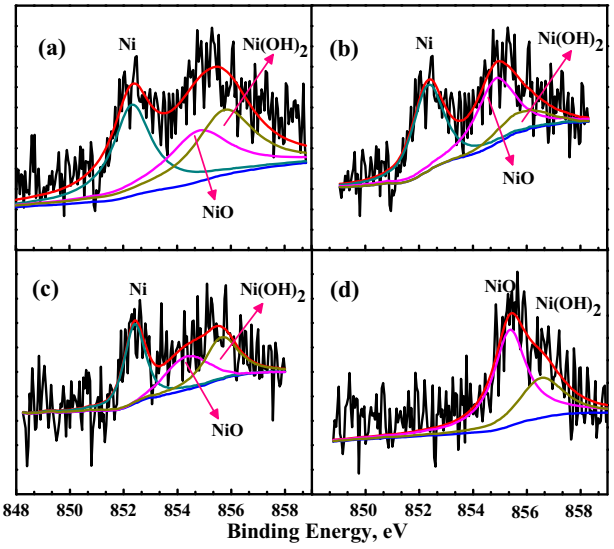

Fig. 6. XPS spectra of Ni $2p_{3/2}$ of the passive film formed on 2507 duplex stainless steel in air (a), and at 0 V_{SCE} (b), 0.3 V_{SCE} (c) and 0.9 V_{SCE} (d) potentials.

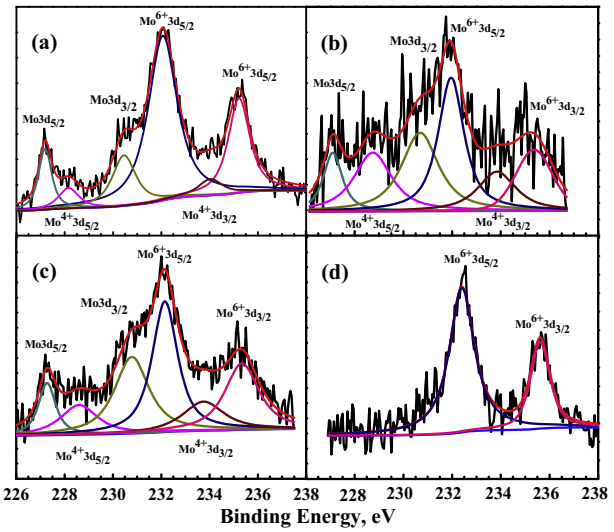

Fig. 7. XPS spectra of Mo 3d of the passive film formed on 2507 duplex stainless steel in air (a), and at 0 V_{SCE} (b), 0.3 V_{SCE} (c) and 0.9 V_{SCE} (d) potentials.

Mo (Mo_{met}, 227.4 eV), six-valent Mo (Mo^{6+}, 232.2 eV) and the four-valen Mo (Mo^{4+}, 228.8 eV).

The spectra for the passive film formed at 0.9 V_{SCE} applied potential (Figs. 4–7) indicate different film compositions of the film formed in air and at 0 or 0.3 V_{SCE} applied potentials. In the Fe $2p_{3/2}$ spectra there are no Fe peak, and the primary constituents of the passive film are FeO (709.9 eV) and FeOOH (712.8 eV), as shown in Fig. 4. In the Cr $2p_{3/2}$ spectra there are two constituent peaks, representing to Cr_2O_3 (576.0 eV) and CrO_3 (578.3 eV), while there are no $Cr_{(met)}$ peaks, and the concentration of the Cr_2O_3 becomes the least, as shown in Fig. 5. Compared with passive films formed in air and at 0 and 0.3 V_{SCE} applied potentials, the Ni $2p_{3/2}$ spectra indicate no Ni, as shown in Fig. 6. It is observed that only Mo^{6+} is present in the Mo 3d spectra, without $Mo_{(met)}$ and Mo^{4+}, shown in Fig. 7. From the XPS analysis, it could be concluded that the chemical composition of the passive film is significantly changed by passivation, especially at the 0.9 V_{SCE} potential.

Table 3
Binding energies of the primary passive film compounds formed on the 2507 duplex stainless steel obtained from the XPS spectra deconvolution.

Element	Peak	Species/binding energy (eV)
Fe	$2P_{3/2}$	Fe(met)/706.5 eV; FeO/709.9 eV Fe_2O_3/711.5 eV; FeOOH/712.00 eV
Cr	$2P_{3/2}$	Cr(met)/573.80 eV; Cr_2O_3/576.00 eV $Cr(OH)_3$/577.00 eV; CrO_3/578.30 eV
Ni	$2P_{3/2}$	Ni(met)/852.32 eV; NiO/854.02 eV $Ni(OH)_2$/855.78 eV
Mo	$3d_{5/2}$ $3d_{3/2}$	Mo(met)/227.40 eV; Mo^{4+}/228.80 eV; Mo^{6+}/232.20 eV; Mo(met)/231.00 eV; Mo^{4+}/234.20 eV; Mo^{6+}/235.80 eV

4. Discussion

In situ CSAFM observations show that the conductivity of the passive film decreases after passivation at various potentials,

compared with the air-formed film. The conductivity drops sharply with the film formation potential, and the austenite phase has higher current than the ferrite. Meanwhile, the I–V curves reveal the existence of *p*-type or *n*-type semiconducting properties, depending on the film formation potential, owing to different chemical composition of the passive film formed at different conditions. The effect of the film formation potential on the local electrical properties and the semiconductor type can be discussed from the viewpoint of the films' chemical composition change.

The zero-current region on I–V curve corresponds to the band gap energy width of the overlayer [20]. The band gap energy extracted from the I–V curves measurements on the passive film is larger on ferrite than that on austenite (see Fig. 3), which could be related to chromium oxides grown on the ferrite grains. It is known that chromium and molybdenum are present in the ferrite phase, while nickel and manganese are present in the austenite phase [12]. In general, chromium is more easily passivated, and thus the chromium oxide is undoubtedly preferentially formed on the ferrite surface, which is the major element used to form the passive film [36]. Therefore, the lower conductivity on the ferrite phase, in comparison with the austenite phase in duplex stainless steel, is attributed to enriched chromium oxides in the passive film on ferrite. Another reason for the lower conductivity of ferrite phase might be the higher molybdenum content (Table 1), which is found to cause increase in the stability of the passive film and corrosion resistance [37].

On the passive films of duplex stainless steel formed in air and at different potentials, the current maps with corresponding current line profiles and the band gap energies extracted from I–V curves measurements show that the conductivity of passive film is changed by passivation. The highest current occurs in air-formed passive film due to the thinnest metal oxide on the specimen surface, about 1.8 nm [20,12]. It matches the XPS result, where the concentration of $Fe_{(met)}$, $Cr_{(met)}$, $Mo_{(met)}$ and $Ni_{(met)}$ is the highest. Moreover, after specimen is passivated in the solution, the conductivity of passive film decreases and drops rapidly with the increase of the film formation potential. This is because the passive film thickness varies with passivation and increases with the formation potentials, its thickness increases from about 3.5 nm to 5 nm with increasing formation potentials from 0 to 0.9 V_{SCE} [2,38]. This is in agreement with XPS analysis (Figs. 4–7 and Table 3), where oxides concentration and chemical composition of the passive films are dramatically changed by passivation. With increasing potential (from 0 to 0.3 V_{SCE}), the concentration of metallic states of iron, chromium, molybdenum and nickel decreases sharply and some metal oxides increase, such as Fe_2O_3, NiO and the four-valent (Mo^{4+}), which leads to the decrease of the passive film conductivity, consistent with previous reports [31,39]. In particular, the passive film formed at 0.9 V_{SCE} applied potential has no metallic iron, chromium, molybdenum and nickel, while the amount of iron and chromium oxides increased. Also some metal oxides and hydroxides appeared, such as FeOOH, FeO, CrO_3, so the current of this passive film is the lowest, which matches previous work, where the thickness of oxides formed at higher applied potential is the largest, about 5 nm [2].

Based on the I–V curves, the air-formed film and films passivated at 0 and 0.3 V_{SCE} appear as *p*-type semiconductors, while the film formed at 0.9 V_{SCE} exhibits *n*-type semiconducting properties. It is well known that the passive films formed on stainless steel exhibit n- or *p*-type semiconducting properties, related to their chemical composition [2]. Generally, the passive film enriched with Cr_2O_3, FeO, NiO, MoO_2, etc. behaves as the *p*-type semiconductor, attributed to chromium or cation vacancies, while the film enriched with Fe_2O_3, FeOOH, CrO_3, MoO_3, etc. exhibits *n*-type semiconductor properties, attributed to some oxygen vacancies or hydrogen atoms trapped in the film [1,40–43]. The passive film enriched with $Cr(OH)_3$ exhibits a *p*-type semiconductor behavior in air and at 0 V_{SCE}, but changed to an *n*-type semiconductor by increasing the applied potential to 0.3 V_{SCE} and higher, such as 0.9 V_{SCE} [44]. XPS analysis (Figs. 4–7) indicates that the air-formed film and films passivated at 0 and 0.3 V_{SCE} have almost the same composition with different oxides concentration, such as Cr_2O_3, FeO, NiO, Mo^{4+}, resulting in the increase of *p*-type semiconducting properties. However, the composition of the passive film formed at 0.9 V_{SCE} is dramatically changed in comparison with the air-formed and films passivated at 0 and 0.3 V_{SCE}. Specifically, FeOOH, FeO, CrO_3 and Mo^{6+} appeared, matching the *n*-type semiconducting character. Moreover, the peaks of the *p*-type semiconductor oxides, such as Cr_2O_3 and FeO, are remarkably decreased by passivation, while the peaks of the *n*-type semiconductor oxides, such as Fe_2O_3, FeOOH, CrO_3 and $Cr(OH)_3$, are increased with increasing potential. XPS quantitative analysis reveals that the ratio of the *p*-type semiconductor compositions and the *n*-type semiconductor compositions before and after passivation is changed, and decreases with the film formation potential, especially for the film formed at 0.9 V_{SCE}. The ratio for the air-formed film and films passivated at 0, 0.3 and 0.9 V_{SCE} is 7.63, 5.24, 1.03 and 0.49, respectively. These results imply that the film surface is reconstructed by passivation, changing from the *p*-type towards the *n*-type semiconductor, namely the *n*-type character of the passive film increases with the ratio decrease.

5. Conclusions

The CSAFM measurements and XPS analysis were used to characterize the local electrical properties of passive films on duplex stainless steel formed in air and at various potentials. The current maps and band gap energies extracted from I–V curves reveal that the current in the passive film on the austenite phase is higher than on the ferrite phase, due to the higher chromium and molybdenum content in the ferrite phase. The electrical conductivity of the passive film decreases after passivation and drops sharply with increasing potential. The current value is the highest for the air-formed film, and the smallest for the film passivated at 0.9 V_{SCE}. This is due to the changes in the passive film thickness and composition by passivation, confirmed by XPS analysis. The I–V curves obtained from the passive film are asymmetric, which can be used to identify the corresponding semiconductor type of the passive film. The passive film behaves as *p*-type or *n*-type semiconductor, depending on the film formation potential, owing to different chemical composition of the passive film formed at different conditions, also demonstrated by XPS results. CSAFM is a useful tool for characterizing semiconducting passive films with high spatial resolution.

Acknowledgements

The authors acknowledge support from the National Natural Science Foundation of China under Grants Nos. 51271026 and 51161160563.

References

[1] S. Ningshen, U. Kamachi, V.K. Mittal, H.S. Khatak, Corros. Sci. 49 (2007) 481–496.
[2] N.E. Hakiki, Corros. Sci. 53 (2011) 2688–2699.
[3] J.W. Schultze, M.M. Lohrengel, Electrochum. Acta 45 (2000) 2499–2504.
[4] P.J. Antony, R.K. Singh Raman, R. Mohanram, P. Kumar, R. Raman, Corros. Sci. 50 (2008) 1858–1864.
[5] J.S. Kim, E.A. Cho, H.S. Kwon, Corros. Sci. 43 (2001) 1403–1409.
[6] A.D. Paola, F.D. Quarto, C. Sunseri, Corros. Sci. 133 (1986) 1326–1330.
[7] E. Cho, H. Kwon, D.D. Macdonald, Electrochim. Acta 47 (2002) 1661–1667.
[8] J. Robertson, Corros. Sci. 32 (1991) 443–465.
[9] Y.J. Kim, Corrosion 51 (1995) 849–860.

[10] N.E. Hakiki, M. Da Cunha Belo, J. Electrochem. Soc. 143 (1996) 3088–3094.
[11] C.O.A. Olsson, Corros. Sci. 37 (1995) 450–467.
[12] V. Vignal, H. Krawiec, O. Heintz, D. Mainy, Corros. Sci. 67 (2013) 109–117.
[13] C.M. Rangel, T.M. Silva, Electrochum. Acta 50 (2005) 5076–5082.
[14] N.E. Hakiki, M.F. Montermor, M.G.S. Ferreira, M. Da Cunha, Corros. Sci. 42 (2000) 687.
[15] S. Mischler, A. Vogel, H. Mathieu, D. Landolt, Corros. Sci. 32 (1991) 925–931.
[16] M.F. Montemor, M.G.S. Ferreira, N.E. Hakiki, Corros. Sci. 42 (2000) 1635–1641.
[17] J. Gluszek, K. Nitsch, Corros. Sci. 22 (1982) 1067.
[18] K. Azumi, T. Ohtsuka, N. Sato, J. Electrochem. Soc. 133 (1986) 1326.
[19] N.E. Hakiki, S. Boudin, B. Rondot, M. Da Cunha Belo, Corros. Sci. 37 (1995) 1809–1814.
[20] T. Souier, F. Martin, C. Bataillon, J. Cousty, Appl. Surf. Sci. 256 (2010) 2434–2439.
[21] T. Souier, M. Chiesa, J. Mater. Res. 27 (2012) 1580–1588.
[22] D.S. Kong, S.H. Chen, C. Wang, W. Yang, Corros. Sci. 45 (2003) 747–758.
[23] C. Marconnet, Y. Wouters, F. Miseque, C. Dagbert, Electrochim. Acta 54 (2008) 123–132.
[24] F.J. Martin, G.T. Cheek, W.E.O. Grady, P.M. Natishan, Corros. Sci. 47 (2005) 3187–3201.
[25] L.Q. Guo, M. Li, X.L. Shi, Y. Yan, X.Y. Li, L.J. Qiao, Corros. Sci. 53 (2011) 3733.
[26] M. Li, L.Q. Guo, L.J. Qiao, Y. Bai, Corros. Sci. 60 (2012) 76–81.
[27] L.Q. Guo, Y. Bai, B.Z. Xu, W. Pan, J.X. Li, L.J. Qiao, Corros. Sci. 70 (2013) 140–144.
[28] T.W. Kelley, C.D. Frisbie, J. Vac. Sci. Technol. B 18 (2000) 632–636.
[29] A. Alexeev, J. Loos, M.M. Koetse, Ultramicroscopy 106 (2006) 191–199.
[30] NIST online database, <http://srdata.nist.gov/xps/>.
[31] C. Donik, A. Kocijan, J.T. Grant, M. Jenko, A. Drenik, B. Pihlar, Corros. Sci. 51 (2009) 827–832.
[32] P. Jussila, K. Lahtonen, M. Lampima, M. Hirsim, M. Valden, Surf. Interface Anal. 40 (2008) 1149–1156.
[33] H. Luo, C.F. Dong, K. Xiao, X.G. Li, Appl. Surf. Sci. 258 (2011) 631–639.
[34] C.T. Liu, J.K. Wu, Corros. Sci. 49 (2007) 2198–2209.
[35] D.A. Shirley, Phys. Rev. B 5 (1972) 4709–4714.
[36] L.F. Garfias-Mesias, J.M. Skyes, C.D.S. Tuck, Corros. Sci. 38 (1996) 1319–1330.
[37] C.A. Olsson, Corros. Sci. 37 (2005) 467–479.
[38] M.G.S. Ferreira, N.E. Hakiki, M.D. Belo, Electrochim. Acta 46 (2001) 3767–3776.
[39] J. Amri, T. Souier, B. Malki, B. Baroux, Corros. Sci. 50 (2008) 431–435.
[40] S. Ningshen, U.K. Mudali, Electrochim. Acta 54 (2001) 6374–6382.
[41] S. Haupt, H. Strehblow, Corros. Sci. 37 (1995) 43–48.
[42] V.G. Chuprina, I.M. Shalya, I.I. Karpikov, Powder Metall. Met. C 34 (1995) 11–12.
[43] I. Olefjord, L. Wegrelius, Corros. Sci. 31 (1990) 89–94.
[44] J. Kim, E. Cho, H. Kwon, Electrochim. Acta 47 (2001) 415–421.